



Cite this: *Lab Chip*, 2025, 25, 5863

# Spatiotemporal temperature control by holographic heating microscopy unveils cellular thermosensitive calcium signalling

Kotaro Oyama, <sup>a</sup> Ayumi Ishii, <sup>b</sup> Shuhei Matsumura, <sup>b</sup> Tomoko G. Oyama, <sup>a</sup> Mitsumasa Taguchi <sup>a</sup> and Madoka Suzuki <sup>\*c</sup>

Optical microheating technologies have revealed how biological systems sense heating and cooling at the microscopic scale. Sensing is based on thermosensitive biochemical reactions that frequently engage membrane proteins,  $\text{Ca}^{2+}$  channels, and pumps to convert sensing information as the  $\text{Ca}^{2+}$  signalling in cells. These findings highlight the feasibility of thermally manipulating intracellular  $\text{Ca}^{2+}$  signalling. However, how the thermosensitive  $\text{Ca}^{2+}$  signalling would behave, particularly in multicellular systems, remains elusive. In this study, to extend the ability of the spatiotemporal temperature control by optical microheating technologies, we propose holographic heating microscopy. Water-absorbable infrared (IR) laser light is modulated by a reflective liquid crystal on a silicon spatial light modulator (LCOS-SLM). A computer-generated hologram displayed on the LCOS-SLM modulates the spatial phase pattern of the IR laser light to generate predesigned temperature gradients at the microscope focal plane. The holographic heating microscopy visualises how thermosensitive  $\text{Ca}^{2+}$  signalling is generated and propagated in MDCK cells, rat hippocampal neurons, and rat neonatal cardiomyocytes. Moreover, the optical control of the temporal temperature gradient reveals the cooling-rate dependency of  $\text{Ca}^{2+}$  signalling in HeLa cells. These findings demonstrate the extended ability of holographic heating microscopy in investigating cellular thermosensitivities and thermally manipulating cellular functions.

Received 8th July 2025,  
Accepted 19th September 2025

DOI: 10.1039/d5lc00675a

[rsc.li/loc](https://rsc.li/loc)

## Introduction

$\text{Ca}^{2+}$  signalling, a form of inter- and intracellular communication, is involved in various cellular processes such as metabolism, muscle contraction, and neural excitation.<sup>1</sup> The spatiotemporal distribution of cytoplasmic  $[\text{Ca}^{2+}]$  ( $[\text{Ca}^{2+}]_i$ ) in  $\text{Ca}^{2+}$  signalling is controlled by a group of biomolecules such as ion channels, exchangers, pumps, and  $\text{Ca}^{2+}$ -binding proteins. In biochemical reactions in general,<sup>2</sup> the activities of these biomolecules can be thermally modulated. The temperature-sensitive transient receptor potential channel is a prominent example, which is activated within a narrow range of the environmental temperature.<sup>3</sup> The rate of  $\text{Ca}^{2+}$  uptake by sarco-/endoplasmic reticulum  $\text{Ca}^{2+}$  ATPase (SERCA) is increased by heating and *vice versa*.<sup>4,5</sup> Therefore, a

combination of the thermosensitivities of the biomolecules involved in  $\text{Ca}^{2+}$  signalling could lead to intracellular thermosensitive  $\text{Ca}^{2+}$  signalling. However, it is difficult to expect in which manner the thermosensitivity would emerge.

To examine the thermosensitivities of living systems at the subcellular spatial scale, microscopic optical heating has been frequently employed.<sup>6–8</sup> This is mainly because optical microheating technologies have two major advantages for this purpose. First, a micron-sized point heat source can generate a local temperature gradient. The thermal response of biomolecules and cells can be examined to a set of various amplitudes of heat stimulations simultaneously within the field of view of the fluorescence microscope. Second, the local temperature gradient can be generated and decayed within a second or shorter because of quick heat diffusion to the environment surrounding the point heat source. Transient localized heating is usually quicker than global heating of the whole specimen. Therefore, the thermal damage to biomolecules and cells caused by long exposure to heat stress can be minimized or even avoided.

A water-absorbable infrared (IR) light (wavelength, approximately 1450 nm) has been a major option because it is compatible with optical microscopy, including fluorescence  $\text{Ca}^{2+}$  imaging, and the temperature of targeted cells can be

<sup>a</sup> Takasaki Institute for Advanced Quantum Science, National Institutes for Quantum Science and Technology, 1233 Watanukimachi, Takasaki, Gunma 370-1292, Japan. E-mail: [oyama.kotaro@qst.go.jp](mailto:oyama.kotaro@qst.go.jp); Tel: +81 27 335 8671

<sup>b</sup> Department of Chemistry and Biochemistry, School of Advanced Science and Engineering, Waseda University, 3-4-1, Okubo, Shinjuku, Tokyo 169-8555, Japan

<sup>c</sup> Institute for Protein Research, The University of Osaka, 3-2 Yamadaoka, Suita, Osaka 565-0871, Japan. E-mail: [suzu\\_mado@protein.osaka-u.ac.jp](mailto:suzu_mado@protein.osaka-u.ac.jp); Tel: +81 6 6879 8628



selectively controlled with a single-cell resolution.<sup>9–12</sup> In these studies, the IR light was focused into a single spot through an objective lens, creating a single temperature gradient in the field of view. Despite its successful applications, optical heating microscopy still has the potential for further development, enabling more precise spatiotemporal control of local temperature and potentially revealing unexplored cellular sensing abilities. To achieve this, the method requires additional capabilities, such as (i) dynamically switching between multiple localized heat sources within the field of view without moving the specimen, (ii) a wider range of options for spatial temperature distributions, and (iii) a wider range of options for temporal temperature distributions.

Herein, we propose a holographic heating microscopy method based on the reflective liquid crystal on silicon (LCOS)-spatial light modulator (SLM). SLMs, such as the digital mirror device (DMD) and LCOS-SLM, can control light distributions in space.<sup>13</sup> SLMs have been employed in biological applications with an IR laser. Wang *et al.* used DMD for the optical stimulation of cells expressing light-activated receptors.<sup>14</sup> Shirasaki *et al.* introduced a scanner mirror to change the position of heating in a cell sorting chip.<sup>15</sup> Compared with these SLMs, LCOS-SLMs can modulate the phase pattern of light with higher efficiency.<sup>16</sup> The computer-generated hologram (CGH) displayed on LCOS-SLMs allows controlling the distribution of light at the microscopic focal plane. These holographic technologies have been widely applied in optical microscopy systems, such as optical tweezers,<sup>17</sup> multisite two-photon excitation,<sup>18</sup> rapid volumetric imaging,<sup>19</sup> and high-throughput transfection.<sup>20</sup> In the present study, we demonstrate its new abilities in spatiotemporally controlling the microscopic temperature. Ca<sup>2+</sup> signalling was manipulated optothermally to reveal cellular responses to temporal temperature gradients.

## Experimental

### Optical setup of the holographic heating microscope

A polarized IR laser light ( $\lambda = 1475$  nm; AF4B150FK75L; Anritsu) was expanded and collimated with a collimator (F810FC-1550; Thorlabs). A reflective LCOS-SLM (SLM-100; Santec) with  $1440 \times 1050$  pixels modulated the phase of light at each pixel. The irradiation was controlled with a mechanical shutter (SSH-25RA; Sigmakoki) and a controller (SSH-C2B; Sigmakoki). Linear polarizers (LPNIR050-MP2 and LPIREA100-C; Thorlabs) and plano-convex lenses (LA1951-C-ML, LA1608-C-ML, LA1131-C-ML, and LA1509-C-ML; Thorlabs) were used. An aluminium block was placed on a slide glass (S1112; Matsunami Glass). An inverted microscope (IX-83; Olympus) equipped with a four-wavelength high-power LED source (LED4D237; 365/490/565/660 nm; Thorlabs), a custom-made dichroic mirror for the IR laser light (Sigmakoki), and an EMCCD camera (iXon Life 888; Andor Technology) were used. CGH images were generated by the CGH generator (version 1.00.00, Santec).

### IR imaging and temperature measurement

Upconversion nanoparticles were synthesized by a thermal decomposition method using Na(CF<sub>3</sub>COO) and Ln(CF<sub>3</sub>COO)<sub>3</sub> as precursors (Ln = Er<sup>3+</sup> and Yb<sup>3+</sup>).<sup>21</sup> The emission spectrum excited by a 1550 nm CW laser light (70.1 mW; 1550 L-11A-NI-NT-NF; Integrated Optics) was measured with a spectrometer (SILVER-Nova 25 TEC ZAP-D; StellarNet). For IR imaging at the microscopic focal plane, the upconversion nanoparticles in chloroform were spread over a glass-bottom dish (3911-035; AGC Techno Glass) and dried at room temperature.

The temperature gradient was visualised with luminescent thermometer nanosheets, which were fabricated on a glass-bottom dish or a polymer-bottom dish (SF-T-D12; Fine Plus International) according to a previously reported method.<sup>22</sup> Experiments using luminescent thermometer nanosheets were performed in the presence of 2 mL phosphate buffered saline (PBS) in the dishes. The thermometer nanosheets were observed with an excitation filter (BP360-370, Olympus), a dichroic mirror (FF493/574-Di01; Semrock), an emission filter (FF01-512/630; Semrock), and a 10 $\times$  (LMPLN10XIR; Olympus) or a 60 $\times$  objective lens (PLAPON60XOTIRF; Olympus). The laser power of the IR light illuminated by the objective lenses was measured using a thermal power sensor at the sample stage (S175C; Thorlabs).

### Cell culture and Ca<sup>2+</sup> imaging

Animal experiments were approved by the Institutional Animal Care and Use Committee of the National Institutes for Quantum Science and Technology. They were performed in accordance with the Fundamental Guidelines for Proper Conduct of Animal Experiments and Related Activities in Academic Research Institutions under the jurisdiction of the Ministry of Education, Culture, Sports, Science, and Technology of Japan.

MDCK cells (RCB0995) and HeLa cells (RCB0007) were purchased from the RIKEN BRC Cell Bank. Two days before the experiment, MDCK cells were transferred onto a polymer-bottom dish and cultured in Eagle's minimum essential medium (MEM) (M5650; Sigma-Aldrich) containing 10% fetal bovine serum (FBS) (12483020; Thermo Fisher Scientific), 2 mM L-glutamine (G7513; Sigma-Aldrich), 100 U mL<sup>-1</sup> penicillin, and 100  $\mu$ g mL<sup>-1</sup> streptomycin (15140122; Thermo Fisher Scientific) at 37 °C in the presence of 5% CO<sub>2</sub>. HeLa cells on a glass-bottom dish were cultured in Eagle's MEM containing 10% FBS (SH30910.03; HyClone), 2 mM L-glutamine, 100 U mL<sup>-1</sup> penicillin, and 100  $\mu$ g mL<sup>-1</sup> streptomycin (10378016; Thermo Fisher Scientific).

Rat hippocampal neurons were obtained from 19 day embryos of Wistar rats (CLEA Japan) following the published protocol.<sup>23</sup> Moreover,  $4 \times 10^5$  cells were cultured in 2 mL of culture medium composed of Neurobasal Plus Medium (A3582901; Thermo Fisher Scientific), B-27 Plus Supplement (A3582801; Thermo Fisher Scientific), 0.5 mM GlutaMAX Supplement (35050061; Thermo Fisher Scientific), 100 U mL<sup>-1</sup>



penicillin, and 100  $\mu\text{g mL}^{-1}$  streptomycin on a polymer-bottom dish coated with 0.3  $\text{mg mL}^{-1}$  collagen (Cellmatrix Type I-C; Nitta Gelatin) and 0.1  $\text{mg mL}^{-1}$  poly-D-lysine (A-003-E; Merck) for 21 days at 37 °C in the presence of 5%  $\text{CO}_2$ . On day 2 after seeding, 1  $\mu\text{M}$  cytosine-1- $\beta$ -D(+)-arabinofuranoside (030-11951; FUJIFILM Wako Pure Chemical) was added. Half the volume of the culture medium was replaced twice in a week.

Cardiomyocytes were obtained from neonatal Wistar rats (Japan SLC) according to the published protocol.<sup>24</sup> Furthermore,  $1.5 \times 10^4$  cell suspension in 0.15 mL of the culture medium composed of Dulbecco's MEM (08488-55; Nacalai Tesque), 10% FBS (Thermo Fisher Scientific), 4 mM L-glutamine (Sigma-Aldrich), 100  $\mu\text{M}$  sodium pyruvate (P8574, Sigma-Aldrich), 100 U  $\text{mL}^{-1}$  penicillin, and 100  $\mu\text{g mL}^{-1}$  streptomycin in a polymer-bottom dish that had been precoated with 0.3  $\text{mg mL}^{-1}$  collagen was incubated overnight at 37 °C in the presence of 5%  $\text{CO}_2$ . From the next day, cells were cultured in 2 mL of the culture medium containing 100  $\mu\text{M}$  5-bromo-2'-deoxyuridine (B5002; Sigma-Aldrich) for 3 days before the experiments.

On the day of the experiments, the cells were incubated in the culture medium containing 5  $\mu\text{M}$  Cal-520, AM (21130; AAT Bioquest) for 30–90 min at 37 °C in the presence of 5%  $\text{CO}_2$ . After two washes with the imaging solution, cells in the imaging solution (140 mM NaCl, 5 mM KCl, 1 mM  $\text{MgCl}_2$ , 1 mM  $\text{Na}_2\text{HPO}_4$ , 10 mM HEPES, 1.8 mM  $\text{CaCl}_2$ , and 25 mM D(+)-glucose, pH 7.4, adjusted by NaOH) were set on the microscope stage for 10 min to stabilize the temperature before the observation. In the experiments for MDCK, neuron and HeLa cells, the temperature was set at 37 °C using a thermostatically controlled incubator (INUC-KR1-F1; Tokai Hit). To minimise the effect of photobleaching in the analyses, cells after observation were not re-used in other observations. In the experiment for cardiomyocytes, the temperature before heating was set at 26 °C to slow the spontaneous beating and to distinguish between the spontaneous and heat-induced beating clearly. MDCK cells, neurons, and cardiomyocytes were observed with the 10 $\times$  objective lens. HeLa cells were observed with the 60 $\times$  objective lens. Cal-520 was excited by 490 nm light and observed with a mirror unit (U-FBNA; Olympus). In the experiments with 2-APB, 4  $\mu\text{L}$  of DMSO containing 100 mM 2-APB (D9754; Sigma-Aldrich) or DMSO alone was added to 2 mL of imaging solution (final concentration: 200  $\mu\text{M}$  2-APB, 0.2% DMSO). The cells were pre-incubated for at least 30 min before being observed. Electrical stimulation ( $\sim 20 \text{ V cm}^{-1}$ , 10 ms) was applied using an electronic stimulator (SEN-7203; Nihon Kohden) and an isolator (SS-104J; Nihon Kohden).

## Statistics

The Steel–Dwass test was performed using EZR (ver 1.54).<sup>25</sup> The Mann–Whitney *U* test and Friedman test with *post hoc* Wilcoxon–Nemenyi–McDonald–Thompson test were performed using OriginPro2024b (OriginLab). Data are expressed as mean  $\pm$  SD.

## Results & Discussion

### Holographic heating microscope for spatially controlling the microscopic temperature

An LCOS-SLM was employed for the spatial and temporal control of the local temperature under the fluorescence microscope. First, a bitmap image, or “target image,” was prepared, which represents the heat source(s) in the focal plane of the microscope. Then, a CGH image for the target image was created (Fig. 1A). Thereafter, water-absorbable IR laser light ( $\lambda = 1475 \text{ nm}$ ) was irradiated to the LCOS-SLM displaying the CGH image. The modulated light was focused by a planoconvex lens (lens 1 in Fig. 1A) to project the target image on a slide glass that was placed in the conjugate image plane of the microscope. An aluminium block was set on the slide glass to mask the 0th diffraction light at the centre of the projected image. The light passing through the slide glass was finally focused by an objective lens to generate the target image at the focal plane. The heating period was controlled by a mechanical shutter.

As a simple demonstration of holographic heating, single-spot heating at two different locations, double-spot (Fig. 1B) heating, and line heating were examined (Fig. 1C). The target image generated by the IR laser light at the microscope focal plane was visually confirmed by an IR-viewer sheet with upconversion nanoparticles ( $\phi = 100\text{--}300 \text{ nm}$ ,  $\lambda_{\text{ex}} = 1550 \text{ nm}$ ,  $\lambda_{\text{em}} = 528, 542, \text{ and } 662 \text{ nm}$ )<sup>21</sup> (Fig. S1, Movie S1). The full width at half maximum (FWHM), which is widely recognised as a standard parameter for determining the spatial resolution of optical images,<sup>26,27</sup> were 26 and 140  $\mu\text{m}$  for IR optical spatial pattern and  $\Delta T$ , respectively (Fig. S2). The actual temperature distributions visualised by the luminescent thermometer nanosheet appeared to be broader than the IR light distributions owing to thermal diffusion. Therefore, we concluded that the spatial resolution of the temperature manipulation in the current setup was 140  $\mu\text{m}$ .

Next, we varied the distance between the two heating spots to determine the minimum resolvable distance for IR light and  $\Delta T$  (Fig. S3). In the current setup, the spatial resolution was limited by the size of the pixels on the LCOS-SLM, which corresponded to 1.1  $\mu\text{m}$  in the focal plane. According to our results, two heating spots were clearly distinguishable in both the IR and  $\Delta T$  images when the distance between the spots was 220 or 110  $\mu\text{m}$ . However, at a separation of 55  $\mu\text{m}$ , the two spots were hardly resolved in  $\Delta T$ , whereas the two spots were still distinguishable in the IR light images. At a separation of 22  $\mu\text{m}$ , the two spots merged in the IR light image. These thresholds for distinguishing the two spots were consistent with the values of the FWHM for IR and  $\Delta T$  (Fig. S2).

By switching two CGH images of a single spot at different locations, temperature distributions were formed alternatively at different locations on the focal plane (Movie S2). For spot heating, the spatial gradient of the temperature increase,  $\Delta T$ , was a linear function of  $\ln(d)$  ( $\Delta T = A - B \ln(d)$ ), where  $d$  is the distance from the heat source, and A and B are constants. Therefore, the shape of the heat source can be considered cylindrical rather than spherical, as we have previously



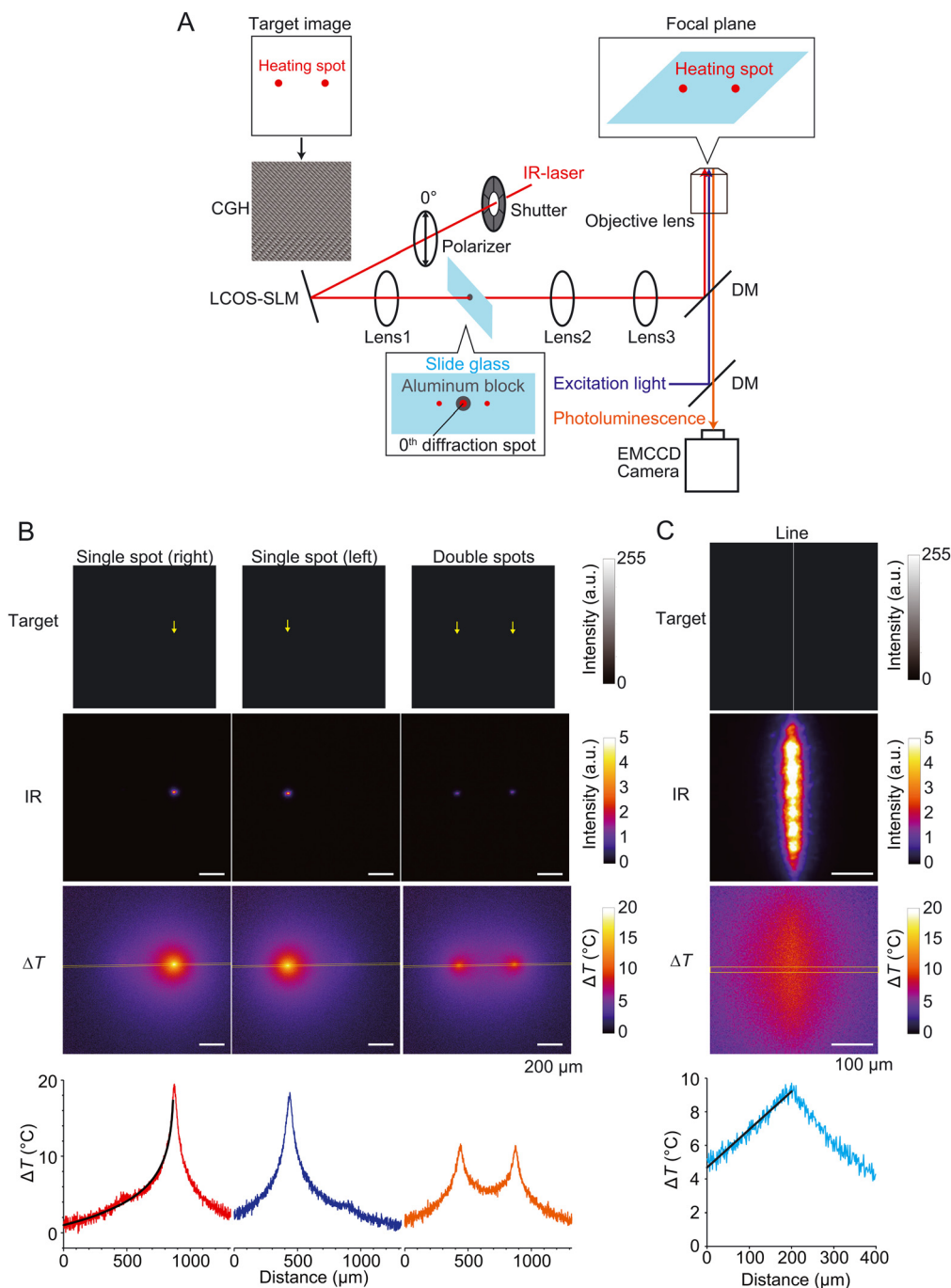


**Fig. 1** Spatial temperature control by the holographic heating microscope. (A) Optical setup for spatially controlling the temperature in the focal plane of the fluorescence microscope. A computer-generated hologram (CGH) image for a bitmap image with two dots was created. Water-absorbable infrared (IR) laser light ( $\lambda = 1475$  nm) was irradiated at a reflective liquid crystal on silicon (LCOS)-spatial light modulator (SLM) displaying the CGH images. The timing and duration of the irradiations were controlled by a mechanical shutter. The IR laser light polarization was aligned with the direction of the long axis ( $0^\circ$ ) of the LCOS-SLM. The modulated light was focused on a slide glass by a planoconvex lens (lens 1) to generate the target image at the focal plane. The 0th diffraction light that appeared as a bright spot at the centre of the generated image was cut by an aluminium block on the slide glass. The light passing through the slide glass was adjusted by two planoconvex lenses (lenses 2 and 3) and focused by an objective lens to generate the target image at the focal plane of the microscope. For the imaging of the luminescent thermometer nanosheets and  $\text{Ca}^{2+}$  signalling, an LED source and an EMCCD camera were used. (B) Top images show target images for single-spot heating on the right or left side or double-spot heating. Yellow arrows indicate the positions of heat sources ( $1 \times 1$  pixel, intensity = 255). The size of target images was adjusted to that of the microscope images for visual purposes. Middle images show the luminescence images of an IR-viewer sheet with upconversion nanoparticles on a glass-bottom dish. The bottom images show the temperature mapping by a luminescent thermometer nanosheet on a polymer-bottom dish in the presence of 2 mL phosphate buffered saline (PBS). Graphs in the bottom show the temperature gradients analysed. The temperature profiles along the yellow rectangles (width,  $12.9 \mu\text{m}$ ) were analysed. The black curve was a fitting by  $\Delta T = -3.67 \ln(d/d_0) + 25.9$  ( $^\circ\text{C}$ ), where  $d$  is the distance from the heat source ( $\mu\text{m}$ ), and  $d_0 = 1$  (in  $\mu\text{m}$ ).  $T_0$ ,  $30^\circ\text{C}$ . Laser power, 12 mW. Scale bars,  $200 \mu\text{m}$ . (C) Same as (B) but for line-shaped heating. The black line is a fitting by  $\Delta T = -0.023 d + 9.2$  ( $^\circ\text{C}$ ).  $T_0$ ,  $30^\circ\text{C}$ . Laser power, 8 mW. Scale bars,  $100 \mu\text{m}$ .





reported.<sup>28,29</sup> For line heating,  $\Delta T$  was a linear function of  $d$  ( $\Delta T = A - Bd$ ), as expected from the geometry. Thus, the holographic heating microscope can spatially control the temperature gradient at the focal plane. See SI Appendix for details.

Under these experimental conditions, heat diffusion from the focal points or areas of the IR laser light occurs mainly *via* the medium. It should be noted that heat transfer in the medium may differ from that in the cells.<sup>30–32</sup> Nevertheless, according to our previous reports, the temperature distribution around the substantially strong heat source generated by the IR laser light is well represented by the values measured by the luminescent thermometer nanosheet under conditions similar to the present study.<sup>23,28,29,33</sup> Considering the agreement between the temperature distributions measured for the point heat source and line heating pattern with the corresponding analytical models (Fig. 1B and C, SI Appendix), we concluded that  $\Delta T$  determined by the luminescent thermometer nanosheet could represent the value in the presence of cells in the current study. Thus, throughout this study,  $\Delta T$  as determined by the nanosheet is used to represent the value both in the absence and presence of cells.

### Spatial manipulation of $\text{Ca}^{2+}$ signalling

Holographic heating microscopy was applied to examine cell type-dependent  $\text{Ca}^{2+}$  signalling in cell populations. We previously reported heat-induced  $\text{Ca}^{2+}$  bursts in the human fibroblast cell line WI-38 during optical heating ( $\Delta T \geq 10^\circ\text{C}$ )<sup>28</sup> and proposed the following mechanism: (i) heating decreases  $[\text{Ca}^{2+}]_i$  and increases  $[\text{Ca}^{2+}]$  in ER ( $[\text{Ca}^{2+}]_{\text{ER}}$ ) quickly because of the acceleration of  $\text{Ca}^{2+}$  uptake by  $\text{Ca}^{2+}$  pump, SERCA<sup>4,5</sup> combined with the decrease in the open probability of  $\text{Ca}^{2+}$  channels, inositol-1,4,5-trisphosphate receptor ( $\text{IP}_3\text{R}$ ), as well as ryanodine receptor ( $\text{RyR}$ ).<sup>34,35</sup> (ii) As the gradient of the electrochemical potential of  $\text{Ca}^{2+}$  between  $[\text{Ca}^{2+}]_i$  and  $[\text{Ca}^{2+}]_{\text{ER}}$  is enhanced, the  $\text{Ca}^{2+}$  uptake by SERCA gradually decreases, and the  $\text{Ca}^{2+}$  outflow from the ER to the cytoplasm through  $\text{IP}_3\text{R}$  is increased. (iii) Finally, the  $\text{Ca}^{2+}$  outflow induces further  $\text{Ca}^{2+}$  release through  $\text{IP}_3\text{R}$  because of the mechanism of  $\text{Ca}^{2+}$ -induced  $\text{Ca}^{2+}$  release (CICR). The results of that study suggest that such a thermosensing system mediated by SERCA and  $\text{IP}_3\text{R}$  would be widely observed in various mammalian cells.

To test this idea, we used Madin–Darby canine kidney (MDCK) cells as a representative epithelial cell line that is frequently employed in cell biology. MDCK cells were stimulated at two locations alternately with 10 s heating and 10 s blank by switching the CGH images of single-spot heating (Fig. 1B). As expected, local heating induced  $\text{Ca}^{2+}$  bursts in the MDCK cells at the target position locally (Fig. 2A and B, Movie S3). Then, second heating was applied at the other coordinates in the focal plane, inducing another local  $\text{Ca}^{2+}$  burst at the location where the second heat source was created. The third heating in the coordinates where the first heating was performed again induced  $\text{Ca}^{2+}$  burst in the similar cell population but with less amplitude than that in

the first heating. Next, we investigated whether the major  $\text{Ca}^{2+}$  release channel was  $\text{IP}_3\text{R}$ , as in WI-38 cells.<sup>28</sup> In the presence of 200  $\mu\text{M}$  2-APB (an inhibitor of  $\text{IP}_3\text{R}$ ), heat-induced  $\text{Ca}^{2+}$  bursts were suppressed significantly (Fig. S4). These results suggest that thermosensitive  $\text{Ca}^{2+}$  signalling *via*  $\text{IP}_3\text{R}$  is a shared property among various mammalian cells.

The temperature changes affect the properties of the fluorescent  $\text{Ca}^{2+}$  indicators in general. In the current case, heating could decrease the Cal-520 intensity because of thermal quenching or increase its intensity of resting  $[\text{Ca}^{2+}]_i$  ( $<100\text{ nM}$ ) due to elevated  $\text{Ca}^{2+}$  affinity, as in the case of fluo-4.<sup>36</sup> As expected, rapid (within a camera frame) decreases in Cal-520 intensity at the initiation of heating and rapid increases at the cessation of heating were observed (Fig. 2B). Similar responses were observed when  $\text{Ca}^{2+}$  bursts were suppressed by 2-APB (Fig. S4B). These phenomena are likely caused by thermal quenching and fluorescence recovery associated with temperature changes. The gradual rise and return of the Cal-520 intensity were noted with a delay from the initiation and cessation of heating, respectively (Fig. 2B). The thermal quenching had no effect on  $\Delta F_{\text{max}} (= F_{\text{max}} - F_0)$ , because the decrease of Cal-520 intensity during heating due to thermal quenching recovered to the initial intensity before heating ( $F_0$ ) immediately after the cessation of heating. Therefore, the increase in the Cal-520 intensity during heating represents the  $[\text{Ca}^{2+}]_i$  increase.

Next, rat hippocampal neurons and neonatal cardiomyocytes were examined. Both cell types communicate *via* synchronized  $\text{Ca}^{2+}$  signalling through electrical coupling. Therefore, the thermosensitive  $\text{Ca}^{2+}$  signalling generated at the heat source is expected to propagate to other regions rapidly (quicker than the order of seconds), which is distinct from the case observed in MDCK cells. Heating of neurons for 2 s, which have been cultured for 21 days until a cellular network was formed, induced  $\text{Ca}^{2+}$  transients in a manner that is comparable to that induced by electrical stimulation (Fig. 2C and D, Movie S4).  $\text{Ca}^{2+}$  transients were observed in nearly all cells in the field of view synchronously, indicating that the heat pulses excited the targeted neurons, and the excitation propagated through the cellular network. Either one or a combination of the following mechanisms can be considered: (i) activation of thermosensitive ion channels such as TRPV1 and TRPV2,<sup>3</sup> (ii) increase in membrane capacitance due to the thermal–mechanical effect,<sup>37–39</sup> and (iii) activation of mechanosensitive ion channels<sup>40</sup> by convection flow during local heating.<sup>23,29,41</sup> Further studies with electrical recording and antagonists for thermo- or mechanosensitive ion channels are required to reveal the details of the mechanism. The possible mechanisms of the decrease in Cal-520 intensity during heating at heating points might be the heat-accelerated  $\text{Ca}^{2+}$  uptake by SERCA and thermal quenching, as discussed above.

The synchronized response was also observed in rat neonatal cardiomyocytes cultured for 4 days after isolation (Fig. 2E and F, Movie S5). A group of cells at the heat source (ROI1) responded to the heating immediately, *i.e.*, the



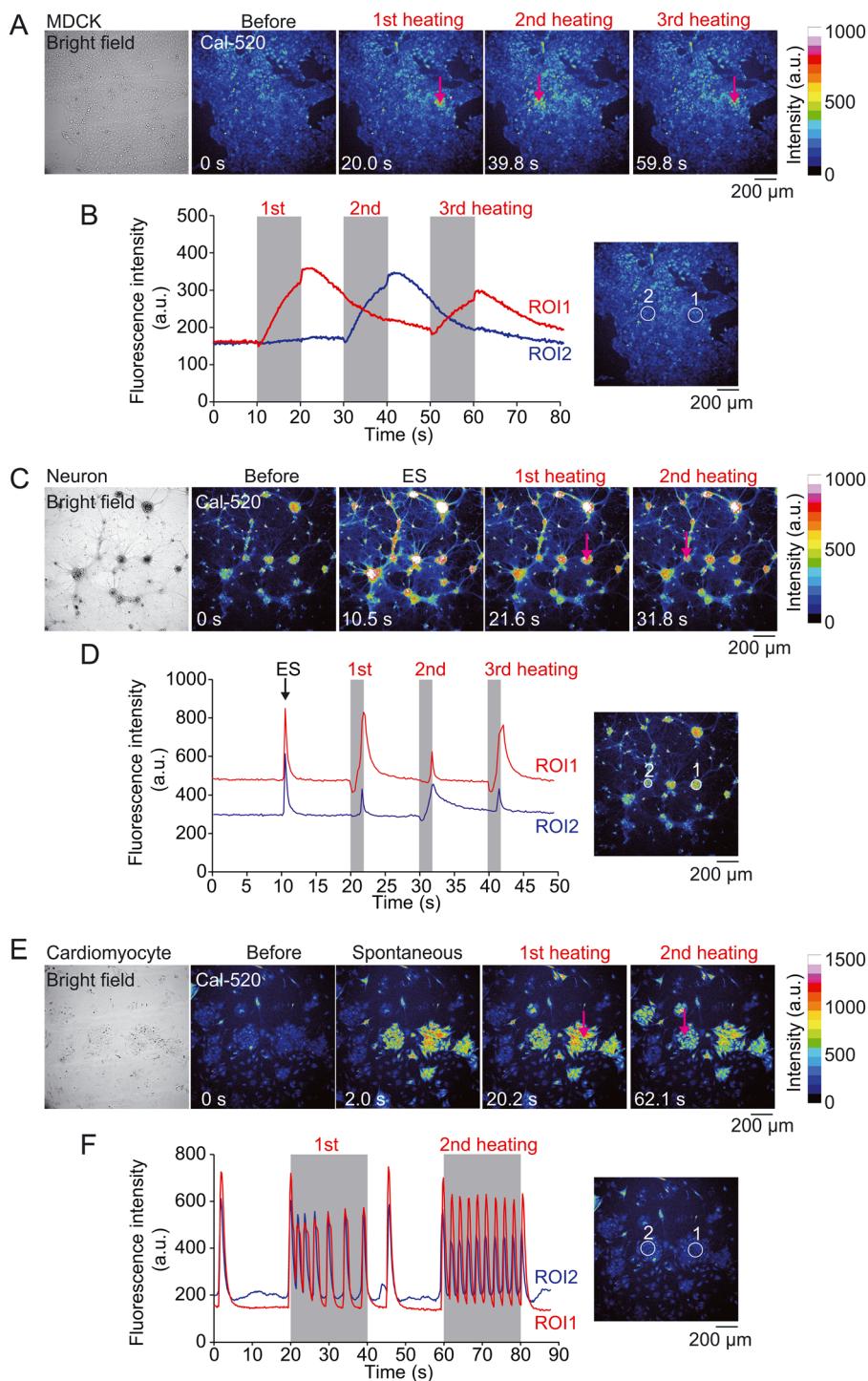


**Fig. 2** Optical manipulation of  $\text{Ca}^{2+}$  signalling by the holographic heating microscope. (A) Bright-field and fluorescence images of MDCK cells stained with the fluorescent  $\text{Ca}^{2+}$  indicator Cal-520. The first, second, and third heatings for 10 s were initiated at 10, 30, and 50 s, respectively, at the locations indicated by magenta arrows.  $T_0$ , 37  $^{\circ}\text{C}$ . (B) Left; time courses of the fluorescence intensities of Cal-520 in MDCK cells responding to optical heating for 10 s. Intensities in two regions of interest (ROIs 1 and 2) shown in the right image were analysed. ROI1 was targeted in the first and third heatings, and ROI2 was targeted in the second heating. (C) Bright-field and fluorescence images of rat hippocampal neurons stained with Cal-520. Electrical stimulation (ES) was applied at 10 s. The first, second, and third heatings for 2 s were initiated at 20, 30, and 40 s, respectively, at the positions indicated by magenta arrows.  $T_0$ , 37  $^{\circ}\text{C}$ . (D) Left; time courses of the fluorescence intensities of Cal-520 in neurons responding to ES or optical heating for 2 s. ROI1 was targeted in the first and third heatings, and ROI2 was targeted in the second heating. The right images show ROI1 and ROI2. (E) Bright-field and fluorescence images of rat neonatal cardiomyocytes stained with Cal-520. The first and second heatings for 20 s were initiated at 20 and 60 s, respectively, at the positions indicated by the magenta arrows.  $T_0$ , 26  $^{\circ}\text{C}$ . (F) Left; time courses of the fluorescence intensities of Cal-520 in cardiomyocytes responding to optical heating for 20 s. ROI1 and ROI2 were targeted in the first and second heatings. The right images show ROI1 and ROI2. Scale bars, 200  $\mu\text{m}$ . The grey bars in B, D and F indicate the period of the heating.  $\Delta T$  at the centre of the heating points was 18–19  $^{\circ}\text{C}$  (Fig. 1B).



frequency of intracellular  $\text{Ca}^{2+}$  transient was increased during heating as observed previously,<sup>42</sup> and cells in the group responded simultaneously. Furthermore, the  $\text{Ca}^{2+}$  response was induced in other nearby groups. Changing the heating location to one of these groups (ROI2) induced a response similar to the primary group (ROI1). The synchronized behaviour of these groups indicates the cellular tight coupling between these cells as in neurons.

Lastly, to highlight the ability of simultaneous illumination at multiple locations with controlled variations in IR light intensity, that is,  $\Delta T$ , we designed three distinct planar heating regions. Here, each heating region was assigned a different grey value in the target image (Fig. 3A, left). Using the holographic heating, we successfully generated IR light distributions with three distinct laser intensities that corresponded to the assigned grey values in the target image (Fig. 3A, middle). Consequently, the local temperature within the heating regions demonstrated three distinct  $\Delta T$  values (ROIs 1 to 3 in Fig. 3A, right, and Fig. 3B). Using this system, we applied multi-region planar heating to MDCK cells and observed three distinct amplitudes of intracellular  $\text{Ca}^{2+}$  bursts in a single measurement, correlating with the  $\Delta T$  at each heating region (Fig. 3C–E). This ability to conduct high-throughput examinations of  $\Delta T$ -dependent intracellular  $\text{Ca}^{2+}$  bursts represents a crucial improvement over previous methods, which typically allow only one  $\Delta T$  at one

heating spot to be examined per measurement. Furthermore, the results demonstrate that the holographic heating microscopy can create spatial patterns of intracellular  $\text{Ca}^{2+}$  levels in multicellular systems.

In summary, the spatial manipulation of the local temperature was employed to demonstrate heat-induced  $\text{Ca}^{2+}$  signalling. Temperature is one of the major parameters governing the functions of the brain and heart. For example, the daily spatiotemporal rhythm in the human brain temperature is related to the age, health, and sex of the individual, and it affects the survival rate from brain injury.<sup>43</sup> We previously reported that optical heating induced cardiac contraction without  $\text{Ca}^{2+}$  transients through the thermal activation of thin filaments.<sup>10,44,45</sup> Therefore, the holographic heating microscope is potentially a useful tool to investigate the effects of temperature on the functions of the brain and heart in *ex vivo* and *in vivo* and further to manipulate them remotely.

### Holographic heating microscope for temporally controlling the microscopic temperature

As the second application of LCOS-SLM, an optical system was designed for temporally controlling the local temperature (Fig. 4A). There has been no control of the cooling rate as the

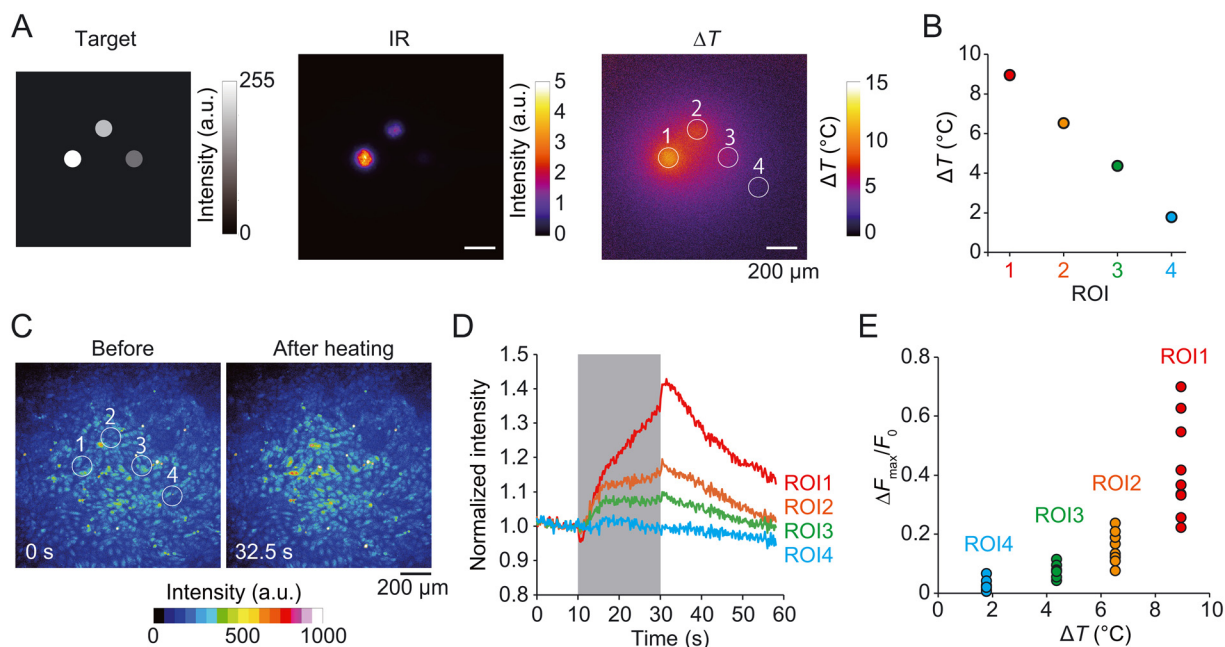


**Fig. 3** Multi-region planar heating with various temperature determines the thermosensitivity of MDCK cells. (A) Left, middle and right images represent the target image for multi-region planar heating, the luminescence image of the IR-viewer sheet with upconversion nanoparticles on a glass-bottom dish, and the map of temperature increase ( $\Delta T$ ) visualised by a luminescent thermometer nanosheet on a polymer-bottom dish in the presence of 2 mL phosphate buffered saline (PBS), respectively. The size of the target image was adjusted to that of the microscope images for visual purposes. Correlation coefficients between the target intensity vs. IR intensity, target intensity vs.  $\Delta T$ , and IR intensity vs.  $\Delta T$  were 0.82, 0.31, and 0.39, respectively. (B) The  $\Delta T$  analysed in four regions of interest (ROIs 1–4) shown in (A). (C) Fluorescence images of MDCK cells stained with the fluorescent  $\text{Ca}^{2+}$  indicator Cal-520. Multi-region planar heating was applied for 20 s, starting at 10 s. (D) Time courses of the fluorescence intensities of Cal-520 in MDCK cells responding to optical heating for 20 s. Intensities in four ROIs (1–4) shown in (C) were analysed. The intensities were normalised to the mean value for 2 s before heating ( $F_0$ ). (E) The maximum changes in the intensities of Cal-520 induced by multi-region planar heating. The maximum change ( $\Delta F_{\text{max}}$ ) was normalised to  $F_0$ .  $T_0$ , 37  $^{\circ}\text{C}$ .



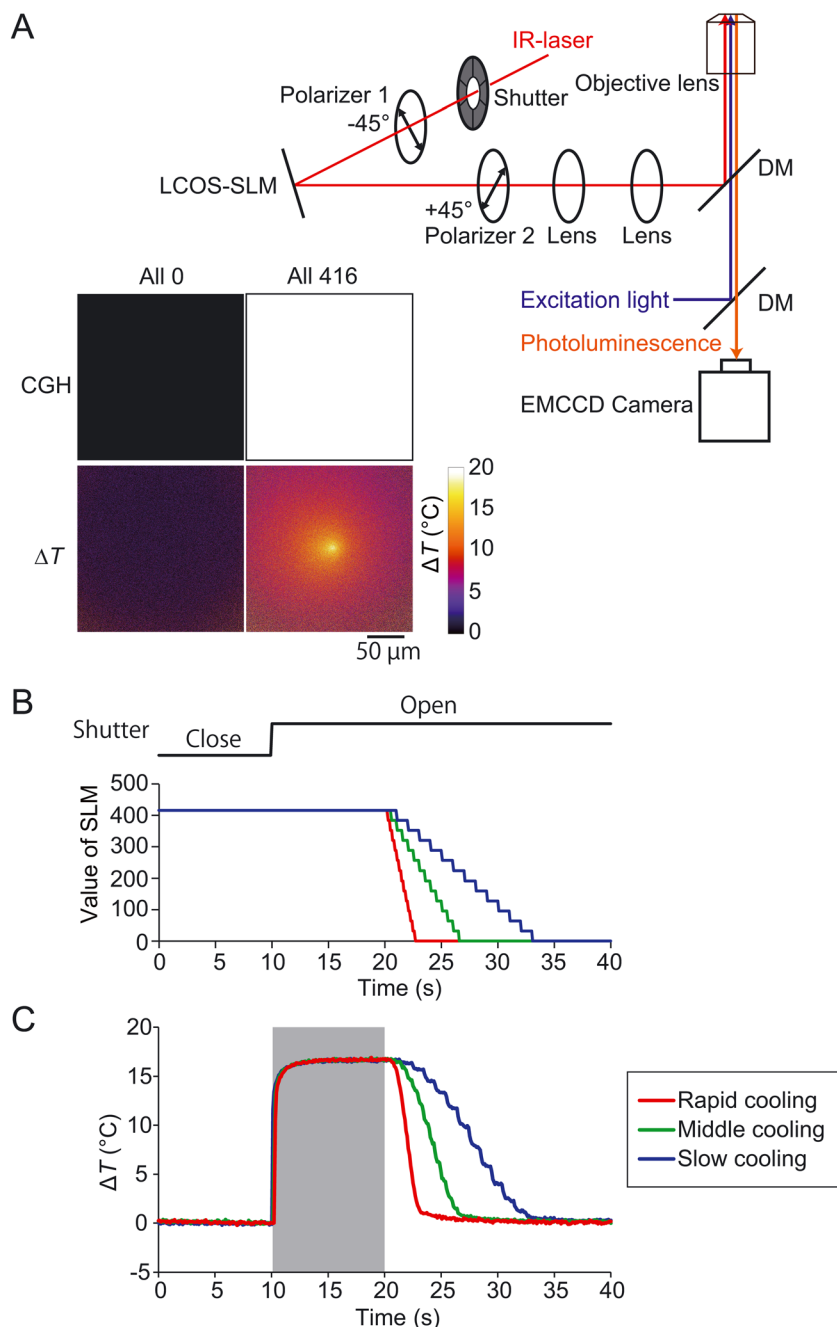


**Fig. 4** Temporal temperature control by the holographic heating microscope. (A) Optical setup for the temporal temperature control. Polarizer 1 was aligned in the  $45^\circ$  direction against the long axis of the LCOS-SLM. Polarizer 2 was set to cut off the IR light without modulation by LCOS-SLM. LCOS-SLM modulates the phase of light in the direction of the long axis of LCOS-SLM. The full-phase inversion gives the maximum transmission through polarizer 2. CGH images show the null (left) and full (right) transmissions of IR light and the corresponding temperature gradients at the microscopic focal plane measured with a luminescent thermometer nanosheet on a glass-bottom dish in the presence of 2 mL phosphate buffered saline (PBS). The intensities at each pixel for null and full were 0 and 416, respectively. (B) Experimental processes for the optical manipulation of the temporal changes in the local temperature. The initial intensity of each pixel in the CGH image was set to 416. Opening a mechanical shutter initiates heating at the focal plane. Following exchanges of 13 CGH images cooled gradually. The periods of exchanges were 0.2, 0.5, and 1.0 s for rapid, middle, and slow cooling, respectively. (C) Temperature changes ( $\Delta T$ ) at the centre of heating. The area within  $5.5\ \mu\text{m}$  from the centre was analysed. A grey bar indicates the period of the maximum heating.  $T_0$ ,  $37^\circ\text{C}$ . Laser power, 13 mW.

cooling process relies on heat diffusion. In the proposed system, two linear polarizers were placed at the paths before and after LCOS-SLM. The first polarizer was aligned in the  $45^\circ$  direction against the long axis ( $0^\circ$ ) of the LCOS-SLM. The

second polarizer was set to cut off the IR light that was reflected without phase modulation by the LCOS-SLM. This setup does not require the aluminium block used in the arrangement shown in Fig. 1 because the non-modulated





light from the LCOS-SLM is blocked by the second polarizer. This design maximises the use of IR light modulated by the LCOS-SLM.

Here, CGH images were created to modulate the phase difference of the IR light. The modulated light passes through the second polarizer in accordance with the following equation:  $I = I_{\max} (\sin \theta)^2$  where  $I$  and  $I_{\max}$  are the light intensity passed through and the maximum intensity, respectively, and  $\theta$  is the phase difference induced by the LCOS-SLM. When the values of the CGH images displayed on the LCOS-SLM were modulated sequentially from 416 to 0, IR light polarization was changed from linear (parallel to the second polarizer with  $\pi/2$  of the phase difference; 100% transparency), elliptical, circular ( $\pi/4$  of the phase difference; 50% transparency), elliptical, and at the end returned to linear (perpendicular to the second polarizer with no phase difference; 0% transparency). In the present study, 14 CGH images with a fixed gap value of 32 from full (value 416) to null (value 0) transmissions were created (Fig. 4B).

Then, the cooling rate was controllable by the dwell time between images. A representative set of rapid, middle, and slow rates of cooling at the centre of the heating spot were achieved, approximately corresponding to  $-5$ ,  $-2$ , and  $-1$  °C s<sup>-1</sup>, respectively, (Fig. 4C). In this experiment, the modulation speed of the CGH images was limited to 200 ms, which was determined by the response speed of the LCOS-SLM system. Although this is notably slower than the modulation speed of DMD-based systems (e.g., up to 32 kHz in models such as the DLP Discover 4100 from Texas Instruments), the slower response speed of the LCOS-SLM has no negative impact on current applications. This is because the time required to reach the steady state for temperature jumps of  $\sim \Delta T = 10$  °C or larger when employing water-absorbable IR light is  $\sim 1$  s (Fig. 4C). For spatial temperature distributions with much smaller  $\Delta T$  or for smaller heat sources, such as those generated using photothermal nanomaterials, the time required to reach the steady state is much shorter, with reported values of  $\sim 0.5$  s<sup>46</sup> or even less than 20 ms.<sup>6</sup> Under these conditions, combining LCOS-SLM with DMD-based systems may provide additional advantages.<sup>47</sup>

### Induction of the Ca<sup>2+</sup> burst is governed by the cooling rate

Finally, temporal temperature modulation was applied to investigate the Ca<sup>2+</sup> burst induced by rapid cooling. Rapid cooling in muscle cells induces Ca<sup>2+</sup> release from the SR *via* ryanodine receptors, and muscle contraction is induced, which is called rapid cooling contracture (RCC).<sup>48</sup> The amplitude of the RCC is dependent on the cooling rate.<sup>49</sup> Similar cooling-rate sensitivity in Ca<sup>2+</sup> bursts was reported in plant cells.<sup>50,51</sup> We previously reported that a transient heating (heat pulse) for 2 s and subsequent cooling induces Ca<sup>2+</sup> bursts in HeLa cells.<sup>41</sup> The proposed mechanism in HeLa cells was that sudden exposure to temperature causes an imbalance in Ca<sup>2+</sup> homeostasis and Ca<sup>2+</sup> release from the ER to the cytosol *via* the IP<sub>3</sub>R receptors. Inspired by these reports, in the present study, we examined the cooling rate

dependency of the Ca<sup>2+</sup> burst in HeLa cells. We heated the HeLa cells for 30 s and then exposed them to recoiling with different cooling rates (Fig. 5A–C; Movies S6–S8). Transient Ca<sup>2+</sup> bursts during heating ( $\Delta F_{\max}/\Delta F_0 > 0.3$ ) were observed in 15% of the cells. Subsequent rapid-rate cooling induced larger Ca<sup>2+</sup> bursts immediately after the cessation of heating than middle- or slow-rate cooling (Fig. 5D and E). Similar results were observed with sequential thermal stimuli applied to the same cells (Fig. S5). These results demonstrate that the Ca<sup>2+</sup> bursts induced by heat pulses were dictated at the cooling rate. Note that the recovery of Cal-520 intensity from thermal quenching is partially included in the increases in  $\Delta F_{\max}/\Delta F'_0$ , where  $\Delta F'_0$  is defined as the mean intensity during the last 2 s of heating, in order to minimize the effect of photobleaching in the analyses. However, this recovery was identical among the three types of recoiling because  $\Delta T$  during heating was constant. Therefore, Cal-520 recovery does not contribute to the differences in  $\Delta F_{\max}/\Delta F'_0$ , and the observed differences in  $\Delta F_{\max}/\Delta F'_0$  among the three recoiling conditions indicate differences in the amplitudes of Ca<sup>2+</sup> bursts induced by recoiling.

Based on current and previous results, the cooling rate dependency of the heat-induced Ca<sup>2+</sup> burst can be explained by a combination of contributions from multiple biomolecules. As the reverse phenomenon of Ca<sup>2+</sup> bursts during heating, the rate of Ca<sup>2+</sup> uptake by the Ca<sup>2+</sup>-ATPase, SERCA, is reduced as the temperature is decreased, and the open probabilities of IP<sub>3</sub>R returns, *i.e.*, is probably increased to the original level before heating. Then, the net Ca<sup>2+</sup> flow (the amount of released Ca<sup>2+</sup> per unit time) from the ER to the cytoplasm could be increased during recoiling, and the Ca<sup>2+</sup> burst is induced due to CICR in IP<sub>3</sub>R. However, when the cooling rate is relatively slow, the recovery rate of the net Ca<sup>2+</sup> flow is also slow, which can be well compensated by the uptake activity of SERCA, exclusion pathways by other Ca<sup>2+</sup> exchangers, and/or buffer function of Ca<sup>2+</sup>-binding proteins.

## Conclusions

This study was conducted to expand the abilities of the spatiotemporal manipulation of the temperature gradient for investigating cellular thermosensitivities and manipulating their functions. The results demonstrated that CGH images displayed on LCOS-SLM modulate the spatial phase pattern of IR light and generate predesigned temperature gradients at the microscopic focal plane. The holographic heating microscope offers extended capabilities compared to conventional methods, where IR light was simply focused into a single spot through an objective lens. This technique surpasses the limitations of previous methods by enabling: (i) dynamic switching between multiple localized heat sources without specimen movement (Fig. 1B), (ii) spatial temperature distributions with various patterns (Fig. 1C and 3A), (iii) multi-region planar heating with different  $\Delta T$  amplitudes (Fig. 3A), and (iv) diverse temporal temperature distributions (Fig. 4). In particular, (iii) and (iv) are not



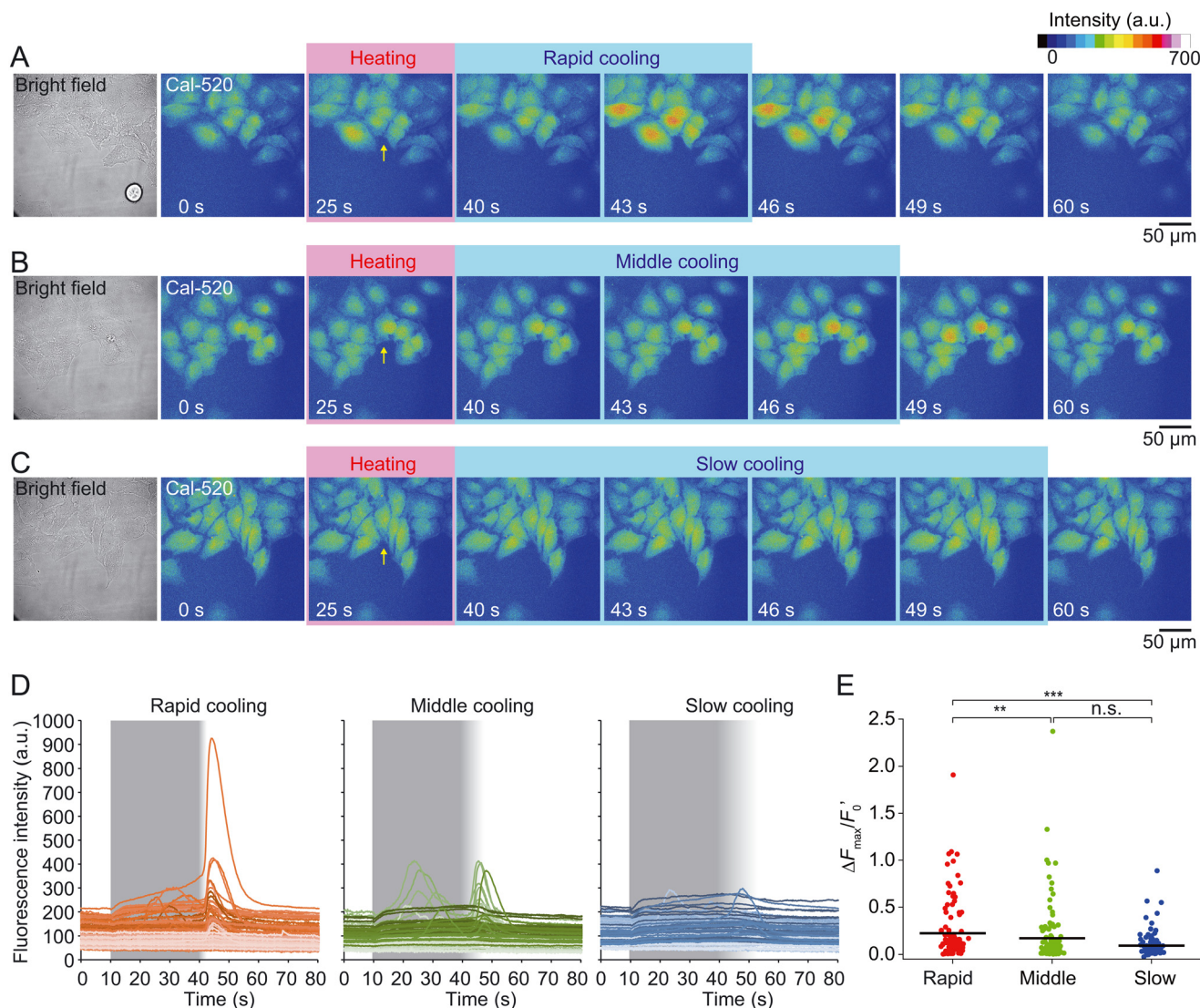


**Fig. 5** The induction of  $\text{Ca}^{2+}$  burst depends on the cooling rate. (A–C) Bright-field and fluorescence images of HeLa cells stained with the fluorescent indicator Cal-520. Optical heating for 30 s was initiated at 10 s. The yellow arrows indicate the locations where the IR light was focused. At 40 s, the cells were exposed to the recooling protocol with rapid (A), middle (B), or slow (C) rates (Fig. 4C). Scale bars, 50  $\mu\text{m}$ . (D) Time courses of the fluorescence intensities of Cal-520 in HeLa cells responding to the thermal stimulation with rapid (left), middle (centre), or slow (right) recooling rates. Grey bars indicate the period of the heating. (E) The maximum changes in the intensities of Cal-520 induced by recooling. To minimize the effect of photobleaching in the analyses, the maximum changes during recooling ( $\Delta F_{\text{max}}$ ) were normalised to the mean intensity during the last 2 s of heating ( $F_0$ ). The cell counts for rapid, middle, and slow recooling were 117, 122, and 112, respectively. The experiments were performed using five dishes, nine observation areas for each stimulus. Some cells exhibited spontaneous  $\text{Ca}^{2+}$  bursts ( $\Delta F_{\text{max}}/\Delta F_0 > 0.3$ ) during heating (15% of the total cells). While these spontaneous  $\text{Ca}^{2+}$  bursts might reduce the amplitude of  $\text{Ca}^{2+}$  bursts after recooling due to reduced  $[\text{Ca}^{2+}]$  in the ER, these cells were included in the analysis to ensure the statistical robustness. The numbers of cells with significant  $\text{Ca}^{2+}$  bursts ( $\Delta F_{\text{max}}/F_0 > 0.3$ ) after recooling were 23 (20%), 16 (13%) and 12 (11%) for rapid-, middle-, and slow-rate cooling, respectively. The amplitudes were compared with the Steel–Dwass test. \*\*  $P < 0.01$ ; \*\*\*  $P < 0.001$ ; n.s., not significant ( $P > 0.05$ ).  $T_0$ , 37  $^{\circ}\text{C}$ ;  $\Delta T$ ,  $8 \pm 1$   $^{\circ}\text{C}$  (mean  $\pm$  SD).

immediately achievable using only DMD. In addition, the diffraction efficiency of LCOS-SLM is higher than that of DMD.<sup>52,53</sup> This advantage is suitable for generating the desired  $\Delta T$  in this setup.

The holographic heating microscope visualised how thermosensitive  $\text{Ca}^{2+}$  signalling is generated and propagated in MDCK cells, rat hippocampal neurons, and rat neonatal cardiomyocytes. For example, the Cal-520 intensity in MDCK cells gradually increased (Fig. 2 and 3), whereas in HeLa cells,

it increased and then decreased during heating (Fig. 5). The holographic heating microscope may help elucidate the mechanistic basis of such the cell type-dependent thermosensitive  $\text{Ca}^{2+}$  responses. Moreover, the optical control of the temporal temperature gradient with the phase modulation of the IR light revealed the cooling-rate dependency of  $\text{Ca}^{2+}$  signalling in HeLa cells. The combination of spatial manipulation of heat sources (Fig. 1 and 3) and temporal manipulation of  $\Delta T$  (Fig. 4) could



generate complicated thermal stimuli with great potential to unveil novel thermosensitivities in living systems.

Although genetically encoded light-sensitive proteins are widely used in optogenetics for the optical manipulation of cellular functions, endogenous thermosensitive systems could be a target of optothermal manipulations.<sup>7</sup> The applications of the holographic heating microscope will not be limited to thermosensitive Ca<sup>2+</sup> signalling. Spatial temperature gradient affects cell morphologies such as membrane extension of HeLa cells<sup>29</sup> and neurite outgrowth<sup>23</sup> and cell division in *Caenorhabditis elegans* embryos.<sup>11</sup> Therefore, the holographic heating microscope might be useful for manipulating cellular morphology, neural networks, and multicellular structures such as spheroids and organoids.

## Author contributions

Conceptualization, K. O. and M. S.; investigation, K. O., A. I., S. M., and T. G. O.; formal analysis, K. O. and M. S.; funding acquisition, K. O., A. I., and M. S. All authors interpreted the results, wrote the original draft, and revised the manuscript.

## Conflicts of interest

The authors declare no conflicts of interest.

## Data availability

Supplementary information is available. See DOI: <https://doi.org/10.1039/D5LC00675A>.

The data supporting this article have been included as part of the Supplementary Information (SI).

## Acknowledgements

We thank Ms. Noriko Uchida (National Institutes for Quantum Science and Technology) and Ms. Noriko Tawara (National Institutes for Quantum Science and Technology) for their technical assistance. This work was supported by the Japan Science and Technology Agency JPMJPR17P3 (to K.O.) and JPMJPR17P2 (to A.I.), JSPS KAKENHI Grant Numbers 22H05054 (to K.O.), and 22H05053 and 25K02242 (to M.S.), Tokuyama Science Foundation (to A.I.), Takeda Science Foundation (to M.S.), and the Collaborative Research Program of Institute for Protein Research, The University of Osaka, CRa-25-01 (to M.S.).

## Notes and references

- 1 M. J. Berridge, M. D. Bootman and H. L. Roderick, *Nat. Rev. Mol. Cell Biol.*, 2003, **4**, 517–529.
- 2 M. Elias, G. Wiczorek, S. Rosenne and D. S. Tawfik, *Trends Biochem. Sci.*, 2014, **39**, 1–7.
- 3 A. Patapoutian, A. M. Peier, G. M. Story and V. Viswanath, *Nat. Rev. Neurosci.*, 2003, **4**, 529–539.
- 4 L. Dode, K. Van Baelen, F. Wuytack and W. L. Dean, *J. Biol. Chem.*, 2001, **276**, 3911–3919.
- 5 A. M. Landeira-Fernandez, J. M. Morrisette, J. M. Blank and B. A. Block, *Am. J. Physiol.*, 2004, **286**, R398–R404.
- 6 K. Oyama, M. Takabayashi, Y. Takei, S. Arai, S. Takeoka, S. Ishiwata and M. Suzuki, *Lab Chip*, 2012, **12**, 1591–1593.
- 7 K. Oyama, S. Ishii and M. Suzuki, *Biophys. Rev.*, 2022, **14**, 41–54.
- 8 L. Sistemich and S. Ebbinghaus, *FEBS Open Bio*, 2024, **14**, 1940–1954.
- 9 Y. Kamei, M. Suzuki, K. Watanabe, K. Fujimori, T. Kawasaki, T. Deguchi, Y. Yoneda, T. Todo, S. Takagi, T. Funatsu, S. Yuba, S. Methods, S. Discussion, S. Note, T. Deguchi, Y. Yoneda, T. Todo, S. Takagi, T. Funatsu and S. Yuba, *Nat. Methods*, 2009, **6**, 79–81.
- 10 K. Oyama, A. Mizuno, S. A. Shintani, H. Itoh, T. Serizawa, N. Fukuda, M. Suzuki and S. Ishiwata, *Biochem. Biophys. Res. Commun.*, 2012, **417**, 607–612.
- 11 J. Choi, H. Zhou, R. Landig, H.-Y. Y. Wu, X. Yu, S. E. Von Stetina, G. Kucsko, S. E. Mango, D. J. Needleman, A. D. T. T. Samuel, P. C. Maurer, H. Park and M. D. Lukin, *Proc. Natl. Acad. Sci. U. S. A.*, 2020, **117**, 14636–14641.
- 12 S. M. Hirsch, S. Sundaramoorthy, T. Davies, Y. Zhuravlev, J. C. Waters, M. Shirasu-Hiza, J. Dumont and J. C. Canman, *Nat. Methods*, 2018, **15**, 921–923.
- 13 A. M. Shaltout, V. M. Shalaev and M. L. Brongersma, *Science*, 2019, **364**, eaat3100.
- 14 S. Wang, S. Szobota, Y. Wang, M. Volgraf, Z. Liu, C. Sun, D. Trauner, E. Y. Isacoff and X. Zhang, *Nano Lett.*, 2007, **7**, 3859–3863.
- 15 Y. Shirasaki, J. Tanaka, H. Makazu, K. Tashiro, S. Shoji, S. Tsukita and T. Funatsu, *Anal. Chem.*, 2006, **78**, 695–701.
- 16 P.-A. Blanche, in *Optical Holography-Materials, Theory and Applications*, Elsevier, 2020, pp. 1–39.
- 17 Y. Hayasaki, M. Itoh, T. Yatagai and N. Nishida, *Opt. Rev.*, 1999, **6**, 24–27.
- 18 V. R. Daria, C. Stricker, R. Bowman, S. Redman and H. A. Bachor, *Appl. Phys. Lett.*, 2009, **95**, 2–5.
- 19 Y. Kozawa, T. Nakamura, Y. Uesugi and S. Sato, *Biomed. Opt. Express*, 2022, **13**, 1702.
- 20 M. Antkowiak, M. L. Torres-Mapa, F. Gunn-Moore and K. Dholakia, *J. Biophotonics*, 2010, **3**, 696–705.
- 21 A. Ishii and T. Miyasaka, *Adv. Photonics Res.*, 2023, **4**, 2200222.
- 22 K. Oyama, M. Gotoh, Y. Hosaka, T. G. Oyama, A. Kubonoya, Y. Suzuki, T. Arai, S. Tsukamoto, Y. Kawamura, H. Itoh, S. A. Shintani, T. Yamazawa, M. Taguchi, S. Ishiwata and N. Fukuda, *J. Gen. Physiol.*, 2020, **152**, e201912469.
- 23 K. Oyama, V. Zeeb, Y. Kawamura, T. Arai, M. Gotoh, H. Itoh, T. Itabashi, M. Suzuki and S. Ishiwata, *Sci. Rep.*, 2015, **5**, 16611.
- 24 S. A. Shintani, K. Oyama, F. Kobirumaki-Shimozawa, T. Ohki, S. Ishiwata and N. Fukuda, *J. Gen. Physiol.*, 2014, **143**, 513–524.
- 25 Y. Kanda, *Bone Marrow Transplant.*, 2013, **48**, 452–458.
- 26 E. Sezgin, *J. Phys.: Condens. Matter*, 2017, **29**, 273001.
- 27 F.-Y. Zhu, L.-J. Mei, R. Tian, C. Li, Y.-L. Wang, S.-L. Xiang, M.-Q. Zhu and B. Z. Tang, *Chem. Soc. Rev.*, 2024, **53**, 3350–3383.





- 28 H. Itoh, K. Oyama, M. Suzuki and S. Ishiwata, *Biophysics*, 2014, **10**, 109–119.
- 29 K. Oyama, T. Arai, A. Isaka, T. Sekiguchi, H. Itoh, Y. Seto, M. Miyazaki, T. Itabashi, T. Ohki, M. Suzuki and S. Ishiwata, *Biophys. J.*, 2015, **109**, 355–364.
- 30 P. Song, H. Gao, Z. Gao, J. Liu, R. Zhang, B. Kang, J.-J. Xu and H. Chen, *Chem*, 2021, **7**, 1569–1587.
- 31 S. Sotoma, C. Zhong, J. C. Y. Kah, H. Yamashita, T. Plakhotnik, Y. Harada and M. Suzuki, *Sci. Adv.*, 2021, **7**, eabd7888.
- 32 K. Lu, T. Wazawa, J. Sakamoto, C. Q. Vu, M. Nakano, Y. Kamei and T. Nagai, *Nano Lett.*, 2022, **22**, 5698–5707.
- 33 S. Arai, S.-C. Lee, D. Zhai, M. Suzuki, Y. T. Chang, E. Reticulum, S. Arai, S.-C. Lee, D. Zhai, M. Suzuki and Y. T. Chang, *Sci. Rep.*, 2014, **4**, 6701.
- 34 F. Protasi, A. Shtifman, F. J. Julian, P. D. Allen, F. Protasi, A. Shtifman, F. J. Julian, P. D. Allen, G. Annunzio, A. Shtifman, F. J. Julian and P. D. Allen, *Am. J. Physiol.*, 2004, **286**, C662–C670.
- 35 R. Sitsapesan, R. A. P. Montgomery, K. T. Macleod, A. J. Williams, B. Y. R. Sitsapesan, R. A. P. Montgomery, K. T. Macleod and A. J. Williams, *J. Physiol.*, 1991, **434**, 469–488.
- 36 M. L. Woodruff, A. P. Sampath, H. R. Matthews, N. V. Krasnoperova, J. Lem and G. L. Fain, *J. Physiol.*, 2002, **542**, 843–854.
- 37 M. G. Shapiro, K. Homma, S. Villarreal, C. P. Richter and F. Bezanilla, *Nat. Commun.*, 2012, **3**, 736.
- 38 Q. Liu, M. J. Frerck, H. A. Holman, E. M. Jorgensen and R. D. Rabbitt, *Biophys. J.*, 2014, **106**, 1570–1577.
- 39 M. Plaksin, E. Shapira, E. Kimmel and S. Shoham, *Phys. Rev. X*, 2018, **8**, 11043.
- 40 W. J. Tyler, *Nat. Rev. Neurosci.*, 2012, **13**, 867–878.
- 41 V. Tseeb, M. Suzuki, K. Oyama, K. Iwai and S. Ishiwata, *HFSP J.*, 2009, **3**, 117–123.
- 42 S. A. Shintani, K. Oyama, N. Fukuda and S. Ishiwata, *Biochem. Biophys. Res. Commun.*, 2015, **457**, 165–170.
- 43 N. M. Rzechorzek, M. J. Thrippleton, F. M. Chappell, G. Mair, A. Ercole, M. Cabeleira, J. Rhodes, I. Marshall and J. S. O'Neill, *Brain*, 2022, **145**, 2031–2048.
- 44 S. Ishii, K. Oyama, T. Arai, H. Itoh, S. A. Shintani, M. Suzuki, F. Kobirumaki-Shimozawa, T. Terui, N. Fukuda and S. Ishiwata, *J. Gen. Physiol.*, 2019, **151**, 860–869.
- 45 S. Ishii, K. Oyama, S. A. Shintani, F. Kobirumaki-Shimozawa, S. Ishiwata and N. Fukuda, *Front. Physiol.*, 2020, **11**, 278.
- 46 Ferdinandus, M. Suzuki, C. Q. Vu, Y. Harada, S. R. Sarker, S. Ishiwata, T. Kitaguchi and S. Arai, *ACS Nano*, 2022, **16**, 9004–9018.
- 47 B. Zhang, P. Peng, A. Paul and J. D. Thompson, *Optica*, 2024, **11**, 227.
- 48 S. Kurihara and T. Sakai, *J. Physiol.*, 1985, **361**, 361–378.
- 49 T. Sakai and S. Kurihara, *Jikeikai Med. J.*, 1974, **21**, 47–88.
- 50 C. Plieth, U. P. Hansen, H. Knight and M. R. Knight, *Plant J.*, 1999, **18**, 491–497.
- 51 J. Nagel-Volkmann, C. Plieth, D. Becker, H. Lüthen, K. Dörffling and H. Lu, *J. Plant Physiol.*, 2009, **166**, 1955–1960.
- 52 H. Yu, J. Park, K. Lee, J. Yoon, K. Kim, S. Lee and Y. Park, *Curr. Appl. Phys.*, 2015, **15**, 632–641.
- 53 S. Turtaev, I. T. Leite, K. J. Mitchell, M. J. Padgett, D. B. Phillips and T. Čížmár, in *Proc. SPIE 10932, Emerging Digital Micromirror Device Based Systems and Applications XI*, ed. M. R. Douglass, B. L. Lee and J. Ehmke, SPIE, 2019, p. 1093203.

